scientific reports

Check for updates

OPEN

New insights of cerium oxide nanoparticles in head and neck cancer treatment

Elif Tarakci[1,2,10], Sahra Esmkhani[1,3,4,10], Jamila Bayramova[1,3,4,10], Feride Melisa Bilgin[1], Kubra Kidik[1,2], Sevin Adiguzel[5], Yigithan Tufan[6], Ahsen Morva Yilmaz[1], Hulya Yilmaz[5], Ozgur Duygulu[7], Serpil Harbeck[8], Batur Ercan[6], Filiz Kaya[1], Digdem Aktoprakligil Aksu[1], Hulya Yazici[3,4,9] & Hilal Yazici[1]✉

Head and neck cancer (HNC) is a genetically complex cancer type having treatment difficulties due to affecting multiple organs in complex anatomical sites. Radiotherapy resistance, chemotoxicity, post-surgery disability makes HNC treatment more complicated. Therefore, there is need to developed new treatment approaches. Nanoparticle-based therapies especially cerium oxide nanoparticles with its anti-cancer features, high catalytic activity, anti- or pro-oxidant and radio-protective properties give a boon for HNC treatment. In the current study, two dextran-coated cerium oxide nanoparticles (Dex-CeNPs) namely SD1 and SD2 were synthesized and characterized by using two types of dextran (D1 and D2) having distinct molecular weights and branching characteristics to understand their potential as a new HNC treatment strategy while evaluating the role of dextran type. The effectivity of the SD1 and SD2 on the HNC cell lines (A253, SCC-25, FaDu) were investigated by analyzing their cytotoxicity, genotoxicity, reactive oxygen species (ROS) generation properties. Low IC_{50} value, high ROS generation and stability profiling of SD2 compared to SD1 indicates the distinct function of dextran type on Dex-CeNPs effectivity on HNC. To better elucidate the effectivity of SD2, flow cytometry analysis and pro-apoptotic (TP53, CASP3, BAX) and anti-apoptotic (Bcl-2) gene expression profiling were investigated in detail. The findings indicate that SD2 exhibits an influence on head and neck cancer cells via the apoptotic pathway. Our research sets the framework for the development of Dex-CeNPs as remarkable nanotherapeutic candidates for treatment of head and neck cancer.

Keywords Cerium oxide nanoparticle, Dextran coated nanoceria, Nanotherapeutics, Head and neck cancer

Head and neck cancer (HNC) is a highly complex and malignant disease that affects numerous vital organs in complex anatomical regions, leading to 400,000 fatalities and 800,000 new cases annually[1]. Tumor genetic heterogeneity, environmental etiologies, and anatomical features create significant limitations in HNC treatment[2,3]. New and current treatment strategies for HNC require multidisciplinary approaches, including surgery, radiotherapy, chemotherapy, immunotherapy and targeted therapy[4]. Although surgery as a conventional method is one of the preferable treatment strategies for most cancers, anatomical difficulties limits this approach for HNC. In addition to surgical difficulties, anatomical deformation has highly negative effect on patients life quality[5]. Radiotherapy, either alone or in combination with other therapies, is currently an applicable approach, albeit with associated drawbacks in less invasive and selective features. Moreover, targeted therapies are a new encouraging era offering additional strategies with a powerful capacity to maximize tumor regression while minimizing surrounding tissue damage[6]. For example, Cetuximab, Pembrolizumab, and Nivolumab are currently

[1]Climate Change and Life Sciences, Biotechnology Research Group, TUBITAK-Marmara Research Center, 41470 Gebze, Kocaeli, Turkey. [2]Department of Biomedical Engineering, Yeditepe University, 34755 Istanbul, Turkey. [3]Department of Cancer Genetics, Oncology Institute, Istanbul University, 34295 Istanbul, Turkey. [4]Division of Cancer Genetics, Department of Basic Oncology, Health Science Institute, Istanbul University, 34093 İstanbul, Turkey. [5]Nanotechnology Research and Application Center (SUNUM), Sabanci University, 34956 Istanbul, Turkey. [6]Department of Metallurgical and Materials Engineering, Middle East Technical University, 06800 Ankara, Turkey. [7]Materials Process Technologies, Metallic and Structural Materials Group, TUBITAK-Marmara Research Center, 41470 Gebze, Kocaeli, Turkey. [8]Materials Process Technologies, CBRN Defence Technologies Research Group, TUBITAK-Marmara Research Center, 41470 Gebze, Kocaeli, Turkey. [9]Department of Medical Biology and Genetics, Medical Faculty, Istanbul Health and Technology University, 34275 İstanbul, Turkey. [10]Elif Tarakci, Sahra Esmkhani and Jamila Bayramova contributed equally to this work. ✉email: hilal.yazici@tubitak.gov.tr

FDA-approved monoclonal antibody-based targeted therapy drugs for HNC[7]. However, low response rates and frequent resistance acquisition to these targeted-therapeutic methods are constraints in patient treatment[8,9]. Therefore, new therapeutic approaches need to be developed to overcome the limitations of current treatments.

Applying nano-medicines for cancer therapy is a rapidly developing field mainly related to their multifunctional features as longer blood circulation, better tissue accumulation, and anti-cancer properties for drug delivery (e.g., small molecules, protein, gene), diagnosis and imaging[10]. Therefore, nanoparticle-based approaches with their unique physicochemical properties may have a potential to limit the high risk of recurrence, metastasis and eliminate intrinsic or acquired therapeutic resistance by increasing the survival rate of HNC patients[3,11].

Among them, cerium oxide nanoparticles (CeNPs) possess a unique "oxidation switch" that makes them highly effective in scavenging reactive oxygen species (ROS)[12]. Due to oxidation switch properties, CeNPs possess catalase, superoxide dismutase (SOD), oxidase, peroxidase, and phosphatase mimic capabilities that depend on ROS, thereby further enhancing their effectiveness[10,13].

The oxidation switch occurs when Ce^{+4} is reduced to Ce^{+3} on the surface of the crystalline lattice structure and is closely related to engineer defects and surface chemistry[14]. The surface chemistry of CeNPs is primarily influenced by factors such as synthesis methods, coating types, and the nanoparticle microenvironment, which includes variables like pH and ionic strength[15]. These factors cause significant change in physicochemical properties of CeNPs, such as particle size, charge, aggregation, and etc., all of which impact their biological interactions[16]. Hence, understanding the various properties and characteristics of CeNPs is essential to harness their potential for various applications[12].

Although CeNPs have various advantages, their therapeutic performance faces challenges which arise from their poor solubility in the water, a large number of surface defects and their natural tendency to agglomeration[17]. To avoid complications in biological applications, surface modification of CeNPs with biocompatible polymers is crucial to prevent aggregation, increase the solubility of particles in aqueous solutions and reduce the possible adverse biological response[18]. As biocompatible polymers, Dextran, oleic acid, poly (acrylic acid) (PAA), polyethylene glycol (PEG), and citric acid minimize the nonspecific interaction of NPs with cells and proteins, increasing their bloodstream circulation period in vivo[19]. Until now, a unique anti-cancer activity of Dextran-coated CeNPs (Dex-CeNPs) was shown against malignant melanoma, ovarian, lung, and bone cancers[13,20,21].

In the current study; dextran, which is a complex polysaccharide derived from the condensation of glucose, was chosen as a surface functionalization molecule. Dextran frequently utilized as a surface modifier in the synthesis of colloidal nanoparticles, owing to its remarkable water solubility[22]. On the other hand, using a sugar-derived surface functionalizing agent will facilitate the nanoparticle's uptake into the cancer cell. These cells exhibit heightened preference for glucose consumption compared to normal cells, enhancing the effectiveness of the nanoparticles[23].

In this work, two different Dextran-coated Cerium Oxide Nanoparticles (Dex-CeNPs) were synthesized using the same synthesis methodology. Two types of dextran with different molecular weights (D1: 9–11 kDa from *Leuconostoc mesenteroides* and D2: 6 kDa from *Leuconostoc* spp.) and branching structures were utilized. The dextran (D1) with higher MW has highly branched structure, which makes it become more symmetrical, while the dextran (D2) with lower MW has less branching with less symmetrical configuration. This difference in structure might affect various physiochemical factors in terms of size, charge, Ce^{+4}/Ce^{+3} ratio, coating thickness and stability. Moreover, these features might affect other factors like cellular uptake, drug release profile, and overall therapeutic efficacy in HNC.

The two synthesized Dex-CeNPs by precipitation method, named SD1 (using D1) and SD2 (using D2), were comprehensively characterized by using spectroscopic, thermal, and imaging techniques to investigate their physicochemical properties including absorbance, size, charge, and structures of NPs comparatively. Following, cellular behaviour of SD1 and SD2 via analysis of cytotoxicity and ROS profile against A253, FaDu, and SCC-25 HNC cell lines were examined. Later, flow cytometry and gene expression analysis (Pro-apoptotic (TP53, CASP3, BAX) and anti-apoptotic (Bcl-2) genes) were performed by SD2 with exhibited high toxicity, ROS profiling and stability in comparison to SD1 to address the impact of this molecule on HNC.

In this study, the effect of Dex-CeNPs as an anti-cancer agent against HNC was shown for the first time, opening ways to develop new nanotherapeutics as potential treatment approaches.

Results and discussion

Coating and branching characteristics of dextran affect physicochemical properties and stability of Dex-CeNPs

Initial physicochemical characterization experiments which cover the visualization of the color changes during synthesis process, UV-Vis spectra, Dynamic Light Scattering (DLS) and zeta potentials were performed (Fig. 1). In summary, the first indicator of the successful synthesis is the color changes during synthesis process as observed in Fig. 1a[24]. Each synthesis (SD1 and SD2) was followed up for 18 h. At the end of 1 h, color changes were observed as bright yellow for SD1 and dark brown for SD2 (Fig. 1a, left). In contrast, color changes were observed as dark brown for SD1 and bright yellow for SD2 at the end of the synthesis after 18 h (Fig. 1a, right). The maximum absorbance peak of SD1 and SD2 was observed at 275 and 287 nm respectively via UV-Vis spectra measurements (Fig. 1b). DLS measurements showed that the hydrodynamic diameter of SD1 and SD2 were approximately 10 ± 0.34 nm with 30% ratio and 100 ± 0.4 nm with 35% (Fig. 1c). The zeta potential values of SD1 and SD2 were -0.029 ± 0.015 and 0.0756 ± 0.110 mV as shown in Fig. 1d. The data indicate us SD1 has slightly negative surface charge where SD2 has a slightly positive surface charge.

After initial physiochemical characterization, the Ce^{3+}/Ce^{4+} ratio of SD1 and SD2 were examined using X-ray photoelectron spectroscopy (XPS). Figure 2a and b showed SD1 and SD2 Ce3d deconvoluted XPS spectra respectively. Ce^{4+} peaked at 881.9, 898.0, 900.5, and 906.4 eV, while Ce^{3+} peaked at 885.8 and 903.6. The SD1 contained 66.7% Ce^{4+} and 33.3% Ce^{3+} with a Ce^{3+}/Ce^{4+} ratio of 0.50. SD2 had 59.2% Ce^{3+} and 40.8%

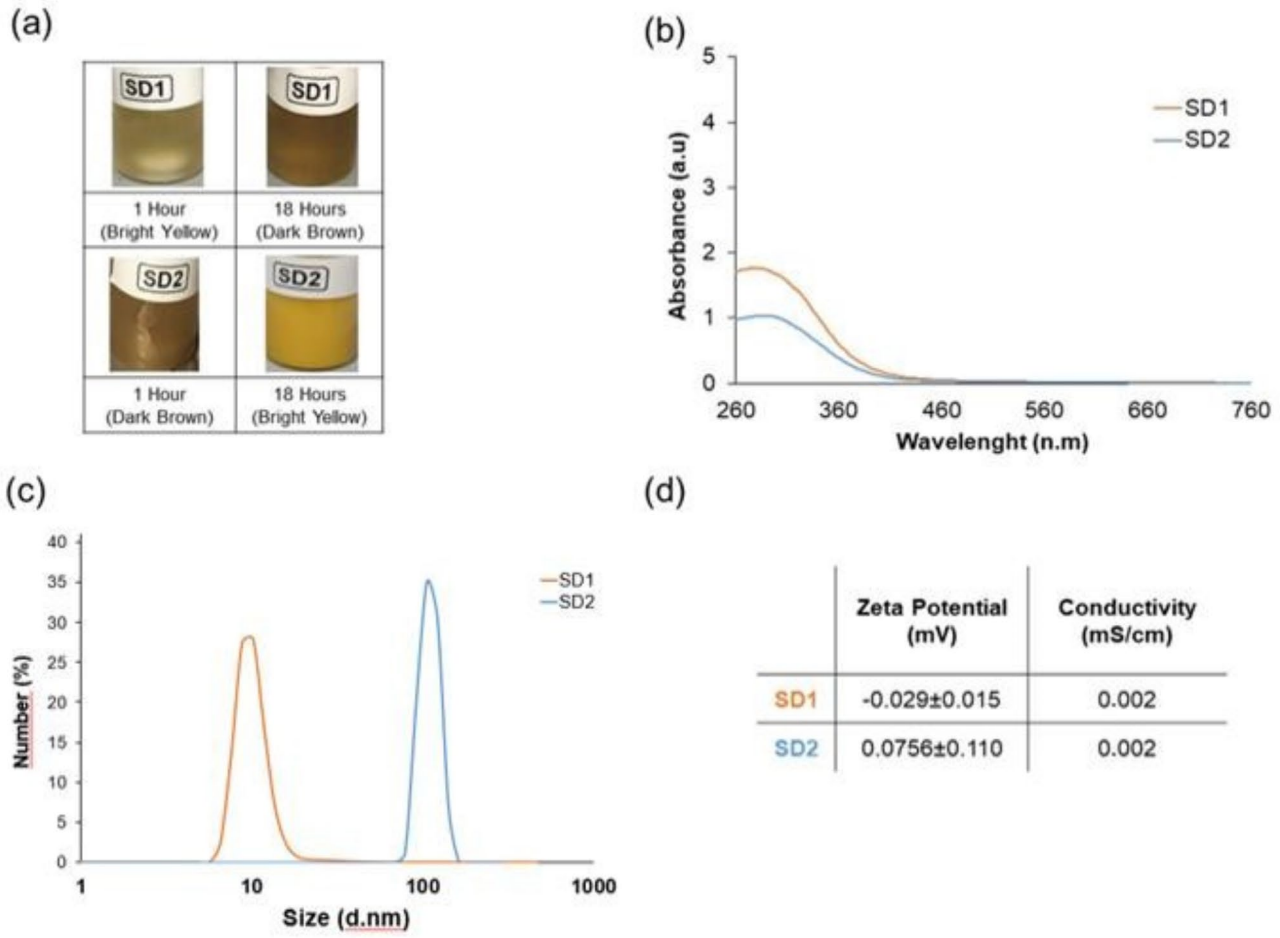

Fig. 1. (**a**) Time-dependent color changes during the synthesis of SD1 and SD2 indicate successful synthesis: SD1 transitions from bright yellow to dark brown, while SD2 changes from dark brown to bright yellow after 18 h. (**b**) UV–Vis spectra (1:100 dilution) reveal maximum absorbance peaks for SD1 and SD2 at 275 and 287 nm, respectively. (**c**) DLS analysis shows hydrodynamic diameters of SD1 and SD2 as approximately 10 ± 0.34 nm with 30% ratio and 100 ± 0.4 nm with 35% nm. (**d**) Zeta potential measurements demonstrate a slightly negative surface charge for SD1 and a slightly positive surface charge for SD2.

Ce^{4+} with a Ce^{3+}/Ce^{4+} ratio of 1.45. As reported in the literature, Li et al. found Ce^{3+}/Ce^{4+} on CeNPs as 0.80 without the dextran coating[25]. Costantino et al. observed Ce^{3+}/Ce^{4+} ratio of 0.42 on cellulose acetate cerium oxide nanoparticle[26]. The distinctive Ce^{+3}/Ce^{+4} ratio seen between SD1 and SD2, in contrast to other cerium oxide nanoparticles reported in the literature, can be attributed to variations in their synthesis and coating methodologies. These results provide important insights into the valence states of cerium oxide nanoparticles and highlight the necessity for further investigation into these states' effects on Dex-CeNPs properties and behavior.

High resolution transmission electron microscopy (HRTEM) imaging was performed to determine Dex-CeNPs' core size and lattice structure. Figure 2c shows HRTEM images of SD1 and SD2 nanoparticle homogeneity with less than 5 nm core diameters. SD2 particles were larger than SD1 in Fig. 2c and correlated with DLS data in Fig. 1c. Both syntheses produced lattice fringes with d-spacing of 0.31 nm and 0.20 nm, which match the (111) and (022) planes of fluid catalytic cracking (FCC) CeO_2 (space group of 225). In order to support the HRTEM results, X-ray diffraction (XRD) measurement was performed to analyze crystal structure of the synthesized nanoparticles XRD patterns show the presence of (111), (220), (311), and (331) planes, typical of a FCC crystal (See Supporting Information, Figure S1)[27]. These results are consistent to each other and in correlation with literature, which shows us FCC structure and homogeneous distribution in solution with, sizes less than 5 nm[14,19]. Moreover, Yazici et al., were synthesized 0.1 M (T-10) Dex-CeNPs with a 3–4 nm core size and FCC structure via the same synthesis strategy followed in this study[21]. Similarly, Hanafy et al. reported that the core size of ethylene glycol-coated cerium oxide nanoparticle, formulated using alkaline precipitation method, was less than 5 nm (with an average of 4 nm) and homogeneously distributed[28].

Performing thermogravimetric analysis (TGA) in nanoparticle characterization is important to understand its thermal stability, quantification of mass changes, purity, and optimization of synthesis processes. The SD1 and SD2 were tested for thermal stability using TGA from 25 to 825 °C with 10 °C interval per minute. Figure 2d

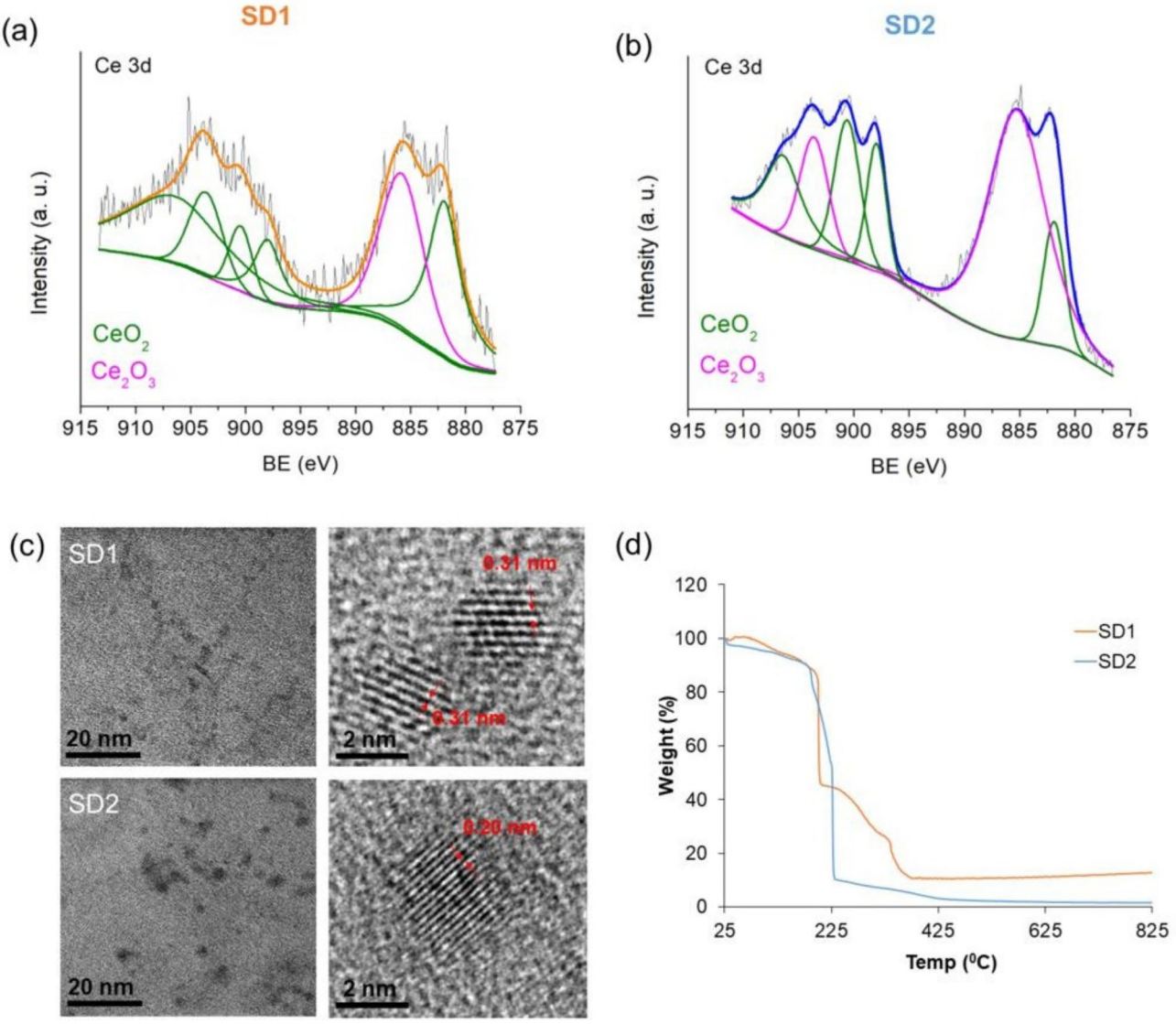

Fig. 2. (**a**,**b**) XPS spectra reveal distinct Ce^{3+}/Ce^{4+} ratios for SD1 and SD2, influenced by their synthesis and coating methodologies. (**c**) HRTEM images of SD1 and SD2 with less than 5 nm core diameters. (**d**) TGA analysis shows thermal stability profiles of SD1 and SD2, which exhibit an 11% weight reduction in the temperature range of 25–182 °C, attributed to the elimination of adsorbed water from the crystalline lattice of cerium oxide. The more branched structure of SD1 contributes to greater heat resistance compared to SD2.

shows TGA graphs of SD1 and SD2. Orange line represents four-stage TGA plots of SD1 decomposition pattern. Weight loss is 13.5% at 25–197 °C, 54% at 204 °C, 72% at 313 °C, and 89.4% at 825 °C in the first four stages. SD2 (blue line) decomposes in three stages: 11% at 25–182 °C, 90% from 182 to 235 °C, and 96.7% at 420–825 °C. SD1 and SD2 decomposition began with water dehydration. SD1 and SD2 lose 11% of their weight between 25 and 182 °C as adsorbed water in cerium oxide's crystalline structure removed. At a temperature of 225 °C, SD1 lost only about 58% of its weight, while SD2 lost nearly 90%. At 825 °C, SD1 loses 89.4% and SD2 96.7% of its weight. SD1 contains larger and more branched dextran (D1: 9–11 kDa), while SD2 contains a smaller molecular weight and less branched dextran (D2: 6 kDa). The more branched structure makes SD1 more heat-resistant than SD2 (Fig. 2d).

There are various examples in the literature to show functionalization/coating of nanoparticles with different type of polymers effect their decomposition profile by analyzing TGA. For instance, Kaygusuz et al. examined the thermal decomposition profile of functionalized alginate-based cerium oxide nanoparticle using TGA. They found that the functionalized cerium oxide nanoparticle gradually decomposed, losing 88% of its starting mass, while non-functionalized cerium oxide nanoparticle preserved 92% of its initial mass[29]. Mohammadi et al. found two weight loss stages in double dextran/PEG-coated iron oxide nanoparticles. The degradation of Dextran and PEG occurred in the second stage (220–440 °C) following the evaporation of H_2O molecules[30].

Attenuated total reflectance fourier-transform infrared (ATR-FTIR) and Raman spectroscopy were employed to analyze the chemical composition of SD1 and SD2. The ATR-FTIR spectra for synthesis without

$Ce(NO_3)_3{\cdot}6H_2O$ (undoped), each dextran type, and Dex-CeNPs (SD1, SD2) were compared to evaluate the success of synthesis process and understand the doping mechanism, as depicted in Fig. 3a and b. The top graphs (pink lines) of Fig. 3a and b present the ATR-FTIR spectra of two dextran types D1 and D2, respectively. The spectra exhibited similarities, showing the expected bands of IR-sensitive vibration modes. However, the intense OH vibration obscured the aliphatic C–H vibration modes of dextrans, and the C–O–C vibration of the glycosidic bridge between saccharide units was observed at around 1158 cm^{-1}.

ATR-FTIR spectra of the doping agent $Ce(NO_3)_3{\cdot}6H_2O$, also shown in the top graphs (black line) of Fig. 3a and c, revealed characteristic nitrate ion (NO_3^-) vibration modes as a broad band between 1470 and 1250 cm^{-1}. The bottom orange and blue lines in each graph represented doped SD1 and SD2 respectively, while the dashed orange and blue lines depicted undoped SD1-SD2 samples respectively. The appearance of vibration modes attributed to NO_3^- ions and the disappearance of absorption bands between 1000 and 1250 cm^{-1}, attributed to C–O–C vibration in the FTIR spectra, indicated successful doping of SD1 and SD2. This suggests that the cerium anion of $Ce(NO_3)_3{\cdot}6H_2O$ binds to the oxygen group of the saccharide ring, consistent with similar reaction mechanisms reported in the literature[13,19].

The ATR-FTIR spectra of D1 and D2 used in the synthesis were very similar, with all the expected bands of IR-sensitive vibrational modes observed, as reported by Naha et al.[19]. However, the OH vibration, which is intense and has a wide band gap, obscured the C–H vibration. The C–O–C vibration at 1158 cm^{-1} corresponded to the glycosidic bonds formed between the saccharides. Additionally, a broad band of characteristic nitrate ion (NO_3^-) vibrational modes was observed between 1470 and 1250 cm^{-1} in the ATR-FTIR spectra of the doping agent $Ce(NO_3)_3{\cdot}6H_2O$. The appearance of the vibrational band attributed to NO_3^- ions in the FTIR plots of dextran-coated SD1 and SD2, and the disappearance of the C–O–C resonance band observed in the dextran plot, confirmed the successful coating of both syntheses with dextran. The presence of a peak at 630 cm^{-1} in the fingerprint region indicated the presence of CeNPs[31], while the vibration band at 1738 cm^{-1} was associated with C=O bonds. Peaks of H_2O (H–O–H) molecular bonds were observed at almost the same positions, at 1640 cm^{-1}

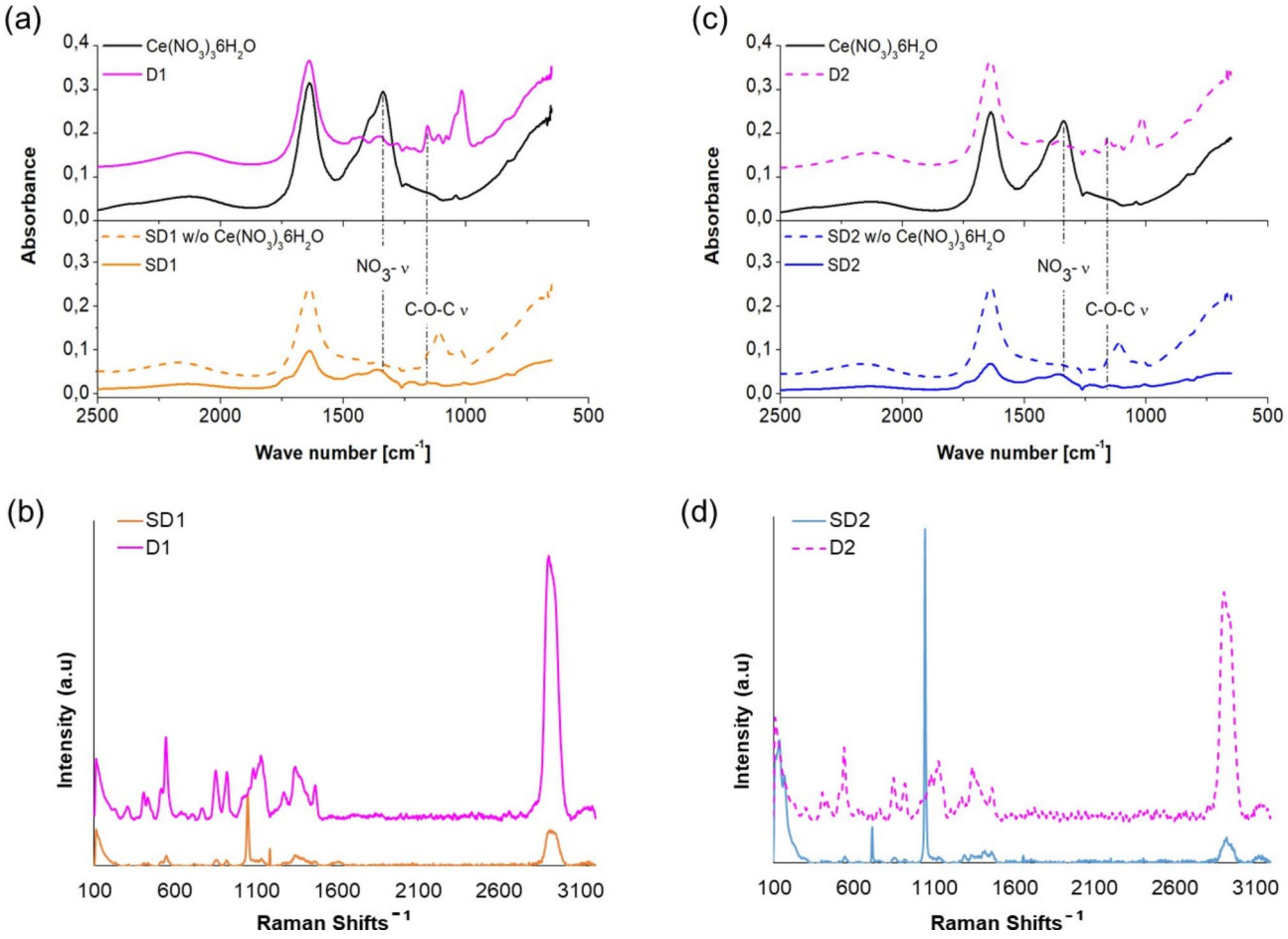

Fig. 3. (**a**) ATR-FTIR spectra of [$Ce(NO_3)_3{\cdot}6H_2O$, (upper black), D1 (upper pink), SD1 without doping (lower dashed orange), SD1 (lower orange)], (**b**) [Raman spectra of SD1 and D1], (**c**) ATR-FTIR spectra of [$Ce(NO_3)_3{\cdot}6H_2O$, (upper black), D2 (upper dashed pink), SD2 without doping (lower dashed blue), SD2 (lower blue)], (**d**) [Raman spectra of SD2 and D2]. ATR-FTIR spectroscopy confirmed the successful dextran coating on cerium oxide, and Raman spectroscopy reinforced these findings by highlighting the high purity of the synthesis process and the effectiveness of the dextran functionalization.

for SD1 and 1639 cm^{-1} for SD2. Furthermore, a weak C–H bending peak at 1467 cm^{-1} was detected[32], along with N–O characteristic vibration bands in the 1340 and 1361 cm^{-1} region[31]. Consequently, the ATR-FTIR spectroscopy results demonstrated the successful coating of dextran on cerium oxide.

Following the ATR-FTIR experiment, Raman spectroscopy analysis was performed on SD1 and SD2, D1 and D2. The comparison of Raman spectra between SD1 (orange line)/D1 (pink line) and SD2 (blue line)/D2 (dashed pink line) in the spectral region of 100 to 3200 cm^{-1} is depicted in Fig. 3b and d, respectively. The Raman spectra of D1 and D2 (pink and dashed pink) exhibited characteristic bands throughout the spectrum range. While the spectral patterns of SD1 and SD2 were similar, the SD2 (blue line) spectrum revealed a new band at 714 cm^{-1} (Fig. 3d). Additionally, the band observed at 1036 cm^{-1} in SD1 shifted to 1050 cm^{-1} in SD2 as shown in Fig. 3d. Both SD1 and SD2 lacked the characteristic Raman band at about 464 cm^{-1}, attributed to the symmetrical stretching mode of Ce–O vibration, indicating successful coating of CeO_2 with dextran. Notably, no fingerprint band for CeO_2 at 464 cm^{-1} was observed in either synthesis (SD1 and SD2), confirming the presence of dextran coating[33]. The Raman spectroscopy analysis results supported the ATR-FTIR data and demonstrated the purity of the syntheses and the successful dextran coating.

Following detail characterization experiment; age dependent changes, which are influenced by various factors within the microenvironment such as light, radiation, moisture, pH, temperature, ionic strength, and concentration[34] were questioned. Therefore, the stability of SD1 and SD2 nanoparticles was analyzed over 6 months at different time intervals using UV-Vis and DLS measurements (see supporting information). 28 days as a critical time period was observed for both syntheses. The change in DLS and UV measurements show us SD2 is more stable than SD1 for over the course of 6 months.

The characterization data except Raman, ATR-FTIR, HRTEM, and XRD was summarized in Table 1 to address the difference between the physicochemical properties of SD1 and SD2. Raman and ATR-FTIR data indicate us successful synthesis of SD1 and SD2 through dextran coating. HRTEM and XRD (in supporting information) data shows the same crystalline structure with very close core size in correlation.

In summary, the more branched structure of the dextran (D1) used for SD1 makes the thinner and entangled coating on cerium oxide. On the other hand, the dextran (D2) used for SD2, which has less and longer branched structure, makes the coating on the cerium oxide thicker and larger. The thinner coating characteristics of SD1 gives smaller absorbance maxima at 275 nm. In contrast, SD2 with thicker coating, bigger size gives absorbance maxima at 287 nm. The OH– groups are in more contact with cerium core for SD1 due to entangled coating, which makes its surface charge slightly positive. These groups are more available on the surface due to disentangled coating for SD2, which makes its surface charge slightly negative. These coating properties of Dex-CeNPs cause different heat stability as such higher for SD1 and lower for SD2. Besides, SD1, with more bounds on the surface, is more prone to change and less stable, whereas SD2, with fewer bounds, is less prone to change and therefore more stable in terms of size.

Dex-CeNPs with no mutagenic potential in the AMES test

Evaluating the genotoxicological profile is necessary to assess the use of any nanoparticles in clinics. This profile can be modulated by physicochemical characteristics of nanoparticles (e.g., size and coating) which also directs internalization of them regarding cellular uptake[35]. Therefore, the genotoxicity profile of Dex-CeNPs were evaluated via Ames test performed with five *S. typhimurium* strains. Since there was no two-fold or more increase in revertant colonies of samples compared to spontaneous and negative control the AMES test of the samples was considered as negative (–) result. It was observed that "SD1 and SD2" are non-mutagenic in these test conditions and in the tested *S. typhimurium* strains (see supporting information)

Characteristic cytotoxicity and ROS profiles of Dex-CeNPs across HNC cell lines temporal and dose-dependent cytotoxicity of Dex-CeNPs in HNC cell lines

The potential of Cerium oxide nanoparticle as an anti-cancer agent has been studied extensively in breast, pancreas, ovarian, lung, colon, and bone cancer cells through various surface modifications[21,36,37]. However, its effectiveness in treating HNC, a challenging cancer type, remains unclear so far. In this study, SD1 and SD2 were tested against HNC cell lines (A253, FaDu, SCC-25) to assess their cytotoxicity profile. These three cell lines were chosen based on their anatomical locations and the prevalent mutations as initial criteria (see supporting information). Specifically, The FaDu cell line is from the pharynx, A253 from the salivary gland, and SCC-25 from the tongue. Among these prevalent mutations TP53, regarded as the guardian of genome, is a pivotal determinant in assessing the effectiveness of various cancer treatment strategies and the most common genetic alteration in head and neck cancer (HNC), occurring in roughly 70% of cases. The molecular profiles of

Characterization method	Results for SD1	Results for SD2
Molecular weight of dextran	9–11 kDa	~6 kDa
UV–Vis spectrophotometry	Peak at approximately 275 nm	Peak at approximately 287 nm
Hydrodynamic diameter	10 nm (30% ratio)	100 nm (25% ratio)
Zeta potential	Slightly positive	Slightly negative
XPS	Higher concentration of Ce^{4+} Ce^{3+}/Ce^{4+} ratio: 0.5	Higher concentration of Ce^{3+} Ce^{3+}/Ce^{4+} ratio: 1.45
TGA	Lost 89% of initial mass	Lost 97% of initial mass
Six-Months Stability	Critical time point: 28 days less stable	Critical time point: 28 days more stable

Table 1. Comparative characterization features of SD1 and SD2.

the selected cell lines and their anatomical regions were comparatively given in the supporting information as Table S1.

Initially, the cytotoxicity was evaluated in a dose and time-dependent manner (on Day 1 and on Day 3) for each cell line. In A253 cells, a dose-dependent change was observed after SD1 and SD2 treatments, whereas time dependence was not significant as shown in Fig. 4a. At 100 µg/mL, SD1 and SD2 had no significant effect on A253 cell viability. However, at 250 µg/mL, SD2 had reduced cell viability by more than 50% on both Day 1 and Day 3, while SD1 had approximately 20% cytotoxicity effect. At higher concentrations (500 and 1000 µg/mL), there is no remarkable change in terms of cell viability in the presence of SD1 and SD2 for both days. In FaDu cells, SD1 and SD2 had different cytotoxicity trend as shown in Fig. 4b. At a concentration of 100 µg/mL, no effect was observed on Day1, while approximately 40% cytotoxicity was observed on Day 3 for SD1. A similar result appears at the concentration of 250 µg/mL. At a concentration of 500 µg/mL, approximately 20% cytotoxicity was observed on Day 1, and 60% cytotoxicity was observed on Day 3. An increased cytotoxic effect (30%) was observed at 1000 µg/mL concentration on Day 1 compare to 500 µg/mL, while a similar trend with 500 µg/mL was observed on Day 3.

On the other hand, SD2 showed very little cytotoxic effect on FaDu cell line up to 500 µg/mL on both Day 1 and Day 3, indicating inefficient long-time effect compared to SD1. At a concentration of 500 µg/mL, SD2 resulted in 40% cytotoxicity on Day 1 and 20% on Day 3. At 1000 µg/mL, SD2 exhibited 70% cytotoxicity on Day 1 and 30% on Day 3 (Fig. 4b). It has been observed that SD1 is much more cytotoxic in long-term exposure compare to SD2, while SD2 was more cytotoxic after Day 1 treatment. It is plausible that the distinct pharmacokinetic properties and temporal dynamics of SD2, in conjunction with the complex cellular microenvironment, may contribute to this temporal shift in cell viability[38].

SD1 and SD2 treated SCC-25 cells showed no significant effect at 100 µg/mL on both Day 1 and Day 3. However, at 250 µg/mL, 500 µg/mL and 1000 µg/mL, SD2 treatment reduced cell viability by about 75% on Day 1. Moreover, cytotoxicity effect was around 80% at 250 µg/mL, and 90% was observed at 500 µg/mL and 1000 µg/mL on Day 3 while SD1 had no significant impact over both days for all concentrations (Fig. 4c).

Depending on cytotoxicity profile observed and reported above, Half-maximal inhibitory concentration (IC_{50}) were calculated as indicated in Table 2. SD1 has IC_{50} (µg/mL) values for A253 (315), FaDu (347), SCC-25 (> 1000), SD2 has IC_{50} (µg/mL) values for A253 (129), FaDu (292), SCC-25 (225).

Evaluation of SD1 in terms of time dependent manner shows us no difference in cell viability for A253, SCC-25 and higher cytotoxic effect over long term exposure for FaDu. The variation in time dependent efficacy of SD2, where exhibited no daily basis cell viability difference for A253; more cytotoxic effect on Day 1 compare to Day 3 for FaDu; slightly less cytotoxic effect on Day 1 compare to Day 3 for SCC-25 was observed.

The change in effectiveness over time of Dex-CeNPs against HNC cell lines can be attributed to the complex dynamics of drug such as initial uptake, cell adaptation, and non-linear dose–response relationships. Moreover, these findings underscore the multifaceted nature of drug–cell interactions and highlight the need for a comprehensive understanding of these factors during the evaluation of potential drug candidates[39].

Ce^{3+}/Ce^{4+} ratio as a key driver of ROS generation of Dex-CeNPs in HNC cell lines

Following, we focused on analyzing ROS generation properties of SD1 and SD2 on HNC cell lines. Figure 4d–f display the ROS fold change after one day of SD1 and SD2 treatment on HNC cells.

In A253 cells (Fig. 4d), ROS production at 100 and 250 µg/mL of SD1 was the same with control group, while 500 µg/mL increased it by 1.5-fold. It was increased around 3-folds at 1000 µg/mL compare to control. For SD2, no fold difference at 100 µg/mL, 3-folds at 250 µg/mL, 2-folds at 500 µg/mL, 1.5-fold difference at 1000 µg/mL compared to control group were observed in terms of ROS generation. ROS enhancement was negligible for SD1 and SD2 around the IC_{50} concentration (315 µg/mL and129 µg/mL respectively) compare to control.

In FaDu cells (Fig. 4e), SD1 had slightly increased ROS production at 100 and 250 µg/mL compared to the control group. This increase escalated to 1.7-fold at 500 µg/mL, and 2-folds at 1000 µg/mL. Conversely, SD2 demonstrate 1.5 fold (100 and 250 µg/mL) and exceeding 1.5-fold across all concentrations on FaDu cells. SD2, at all concentrations, had an impact of more than 1.5-fold on FaDu cells. The IC_{50} values for FaDu cells were 347 µg/mL for SD1 and 292 µg/mL for SD2. Compared to A253 cells, FaDu cells generated more ROS at concentrations around the IC_{50}.

For the SCC-25 cell line (Fig. 4f), SD1 showed no significant impact on ROS generation at all concentrations, while SD2 elicited notable effects with four-folds, six-folds, and five-folds increase in ROS generation at 250, 500, and 1000 µg/mL, respectively. The IC_{50} values for SCC-25 cells were > 1000 µg/mL for SD1 and 225 µg/mL for SD2. Non-signifcant ROS production was observed for SD1 while SD2 showed more than four-folds increase at around IC_{50} concentration for each nanoparticle.

ROS generation for cerium oxide NPs, as nanozymes, is related with the Ce^{3+}/Ce^{4+} ratio on the nanoparticle surface which also defines its mimetic activity of redox enzymes such as SOD, catalase, phosphatase, oxidase peroxidase, and phosphotriesterase. The Ce^{3+}/Ce^{4+} ratio, with Ce^{3+} dominated ratio exhibiting stronger SOD-like activity and with dominated Ce^{4+} ratio have catalase and phosphatase-mimetic activities[40].

In this study, SD1 has a Ce^{3+}/Ce^{4+} ratio of 0.5, while SD2 has a ratio of 1.45, depending on XPS data. This data gives us, SD2 may have a role as superoxide dismutase, whereas SD1 mimics catalase. The correlation between the Ce^{3+}/Ce^{4+} ratio of Dex-CeNPs and ROS generation may change its function though enzymatic behavior as we observed in this study[41,42].

A higher potency and improved efficacy of SD2 as an anti-cancer agent, our subsequent decision to focus on SD2 for further experiments using flow cytometry analysis and gene expression profiling.

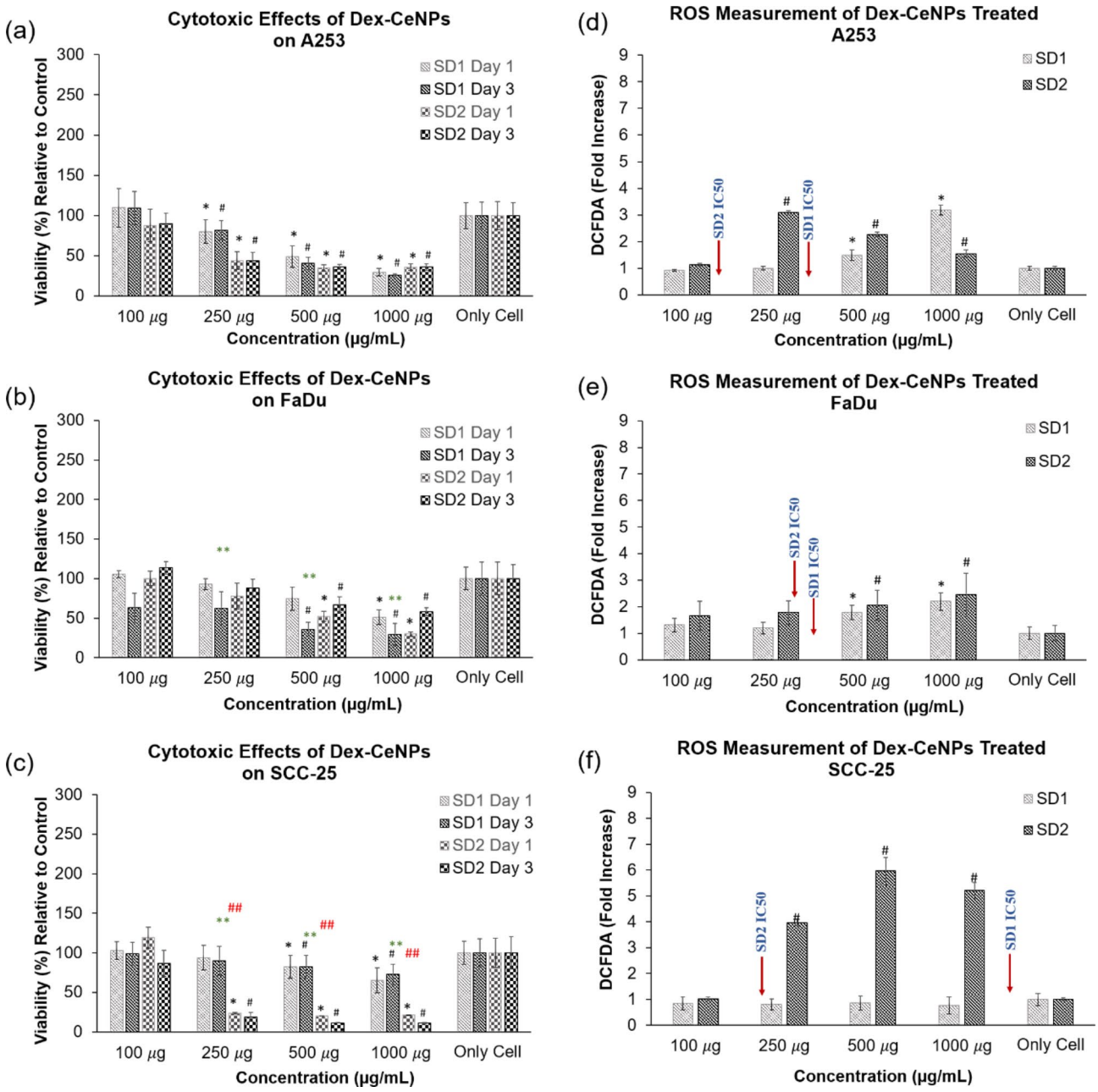

Fig. 4. Cytotoxic properties of SD1 and SD2 against (**a**) A253, (**b**) FaDu, (**c**) SCC-25 cell lines at 100, 250, 500, 1000 µg/mL concentrations after 1 and 3 days of treatment. SD1 and SD2 displayed time and dose-dependent variability across cell lines. *Represents comparison between SD1/SD2 Day 1 and control group for each concentration (p value ≤ 0.05). #Represents comparison between SD1/SD2 Day 3 and control group for each concentration (p value ≤ 0.05). **Represents comparison between SD1, Day 1 and SD2, Day 1 at the same concentration (p value ≤ 0.05). ##Represents comparison between SD1, Day 3 and SD2, Day 3 at the same concentration (p value ≤ 0.05). ROS generation of SD1 and SD2 against (**d**) A253, (**e**) FaDu, (**f**) SCC-25 cell lines at 100, 250, 500, 1000 µg/mL concentrations after 24H of treatment. The variation in ROS production depend on applied dose and the Ce^{3+}/Ce^{4+} ratio between SD1 and SD2. *Represents comparison between SD1 control group and each concentration (p value ≤ 0.001). #Represents comparison between SD2 control group and each concentration (p value ≤ 0.001). **Represents comparison between SD1 and SD2 at the same concentration (p value ≤ 0.001).

Divergent apoptotic and necrotic responses to Dex-CeNPs (SD2) in HNC Cell lines revealed by flow cytometry

Apoptosis, which initiated by 2 main pathways: intrinsic and extrinsic (controlled by pro- and anti-apoptotic regulatory proteins of the Bcl-2 family and Caspases), is a part of the normal physiological process that ensures tissue homeostasis. The regulation of apoptosis was damaged in cancerous cells, which develop "Resistance to

IC_{50} (µg/mL)	SD1	SD2
A253	315	129
FaDu	347	292
SCC-25	> 1000	225

Table 2. IC_{50} values for HNC cell lines.

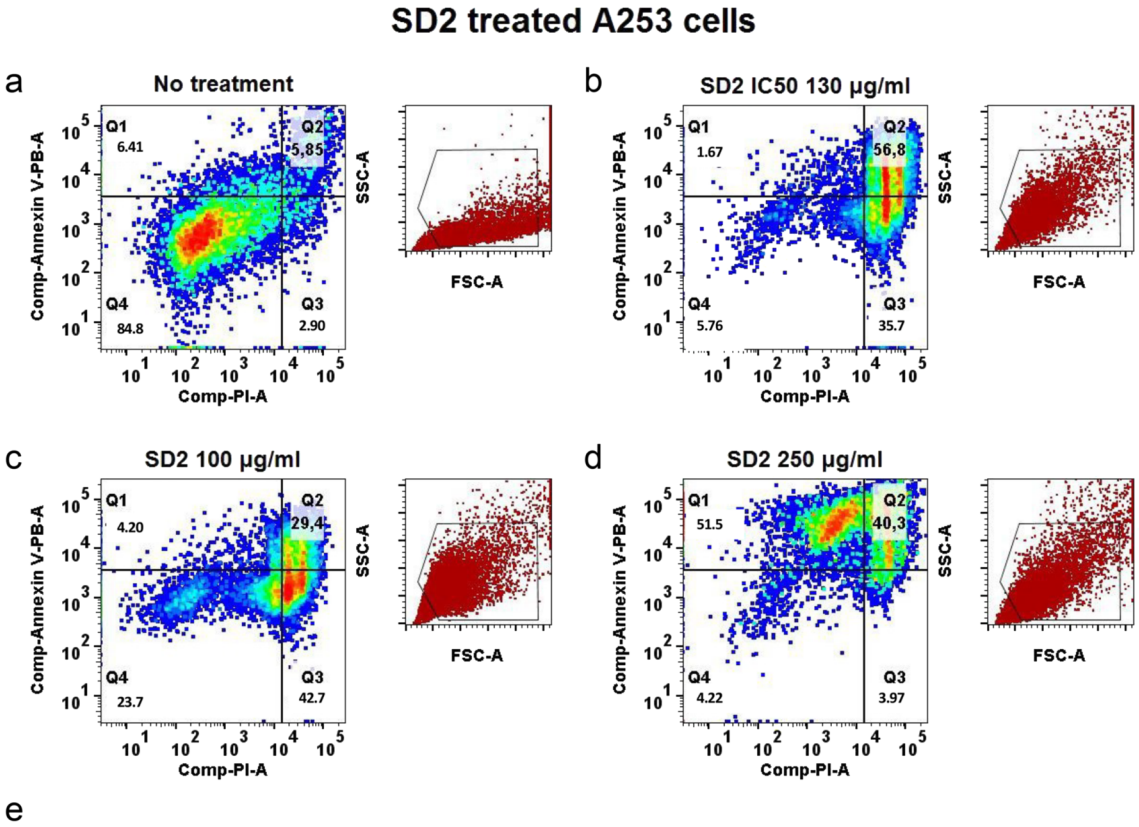

e

		Healthy	Early Apoptosis	Late Apoptosis	Necrosis
	No treatment	90.23% ± 4.72%	3.66% ± 2.39%	4.58% ± 1.37%	1.54% ± 1.38%
SD2	*100 µg/ml*	**13.86% ± 8.52%** ***	4.29% ± 1.92%	**49.4% ± 17.34%** ***	**32.43% ± 8.97%** **
	130 µg/ml (IC50)	**7.73% ± 4.06%** ***	5.01% ± 6.06%	**53.3% ± 3.1%** ***	**33.97% ± 8.53%** **
	250 µg/ml	**14.36% ± 12.99%** ***	**39.43% ± 19.36%** ***	**33.57% ± 20.45%** **	12.66% ± 9.75%

Fig. 5. SD2 predominantly induces late apoptosis in A253 cells at IC_{50} concentration. A253 cells were left (**a**) untreated (negative control) or treated for 24 h with SD2 at (**b**) 100 µg/mL, (**c**) IC_{50}-130 µg/mL, (**d**) 250 µg/mL. Results are expressed as the percentage of cells corresponding to Q1: early apoptotic cells (Annexin V^+/PI^-); Q2: late apoptotic cells (Annexin V^+/PI^+); Q3: necrotic cells (Annexin V^-/PI^+); and Q4: healthy. Cells (Annexin V^-/PI^-). Red dot blots (SSC-A/FSC-A) represent corresponding backgate. Representative example of 5 independent experiments. (**e**) The table refers to the percentage of cells corresponding to each apoptotic level (Mean ± SD). Two-way ANOVA test with Tukey correction across each row indicates statistical significance $^*p < 0.05$, $^{**}p < 0.01$, $^{***}p < 0.001$ vs. control.

cell death"[43]. In the content of this study, Flow Cytometry Analysis and gene expression profiling were performed to understand the apoptotic effect of SD2 in the following sections.

HNC cell line apoptosis profile following SD2 treatment was evaluated with Annexin V/PI double immunostaining. Three different concentrations (IC_{50}, below the IC_{50} and above the IC_{50} which overlaps with the cell viability data) were chosen for flow cytometry analyses in the presence of three cell lines.

Figure 5a illustrates the healthy profile of untreated A253 cells, showing 88.7% viability (Fig. 5e). At a concentration of 100 µg/mL (below IC_{50}), the viability dropped to 16.21% ± 0.33%, ($p < 0.001$) (Fig. 5b,e), at IC_{50}-130 µg/mL it fells to 5.39% ± 0.52%, ($p < 0.001$) (Fig. 5c,e), and at 250 µg/mL (above IC_{50}), it was reduced to 7.04% ± 0.98%, ($p < 0.001$) (Fig. 5d,e).

Interestingly, while there is no significant increase of early apoptotic level at 100 µg/mL and IC_{50}-130 µg/mL concentration (5.23% ± 0.72%, 6.84% ± 0.23% respectively, p = ns), compared to 250 µg/mL (50.6% ± 1.27%, $p < 0.001$). A direct switch to late apoptotic state is detected in lower IC_{50} and IC_{50} conditions (58.2% ± 0.42%, 63.35% ± 4.81% respectively, $p < 0.001$). In 100 µg/mL and IC_{50}-130 µg/mL of SD2, necrotic cells amount are higher than 250 (12% ± 1.07%, $p < 0.001$). These reductions indicate that SD2 induces late apoptosis at IC_{50}.

Figure 6 shows FaDu cell apoptosis profile after SD2 treatment. In all situations, cell amount in early and late apoptosis increase in dose-dependent manner. The necrotic quantities were the same for 250 and 500 µg/mL, while this amount increased at the IC_{50}-290 µg/mL concentration (40% ± 6.65%).

SCC-25 cells exhibit heightened early and late apoptosis percentage in dose-dependent manner like FaDu cells (Fig. 7). Only IC_{50}-220 µg/mL concentration causes considerable necrosis amount in SCC-25 cells (9.61% ± 1.69%, $p < 0.001$).

According to the data presented, although all three cell lines were sensitive to SD2, their response was not necessarily dose-dependent. With below IC_{50} and IC_{50} concentrations of SD2, A253 cells skip early apoptosis and go straight to late stage. Unexpectedly, the highest dose of SD2 induces early apoptosis but not late or necrosis. The IC_{50} concentration had the greatest apoptotic effect on A253 and SCC-25 cell lines. In FaDu and SCC-25 cell lines, SD2 at the below IC_{50} and above IC_{50} concentrations has a milder necrotic effect than IC_{50}. While the highest necrotic cell amount was observed at below IC_{50} concentrations for A253.

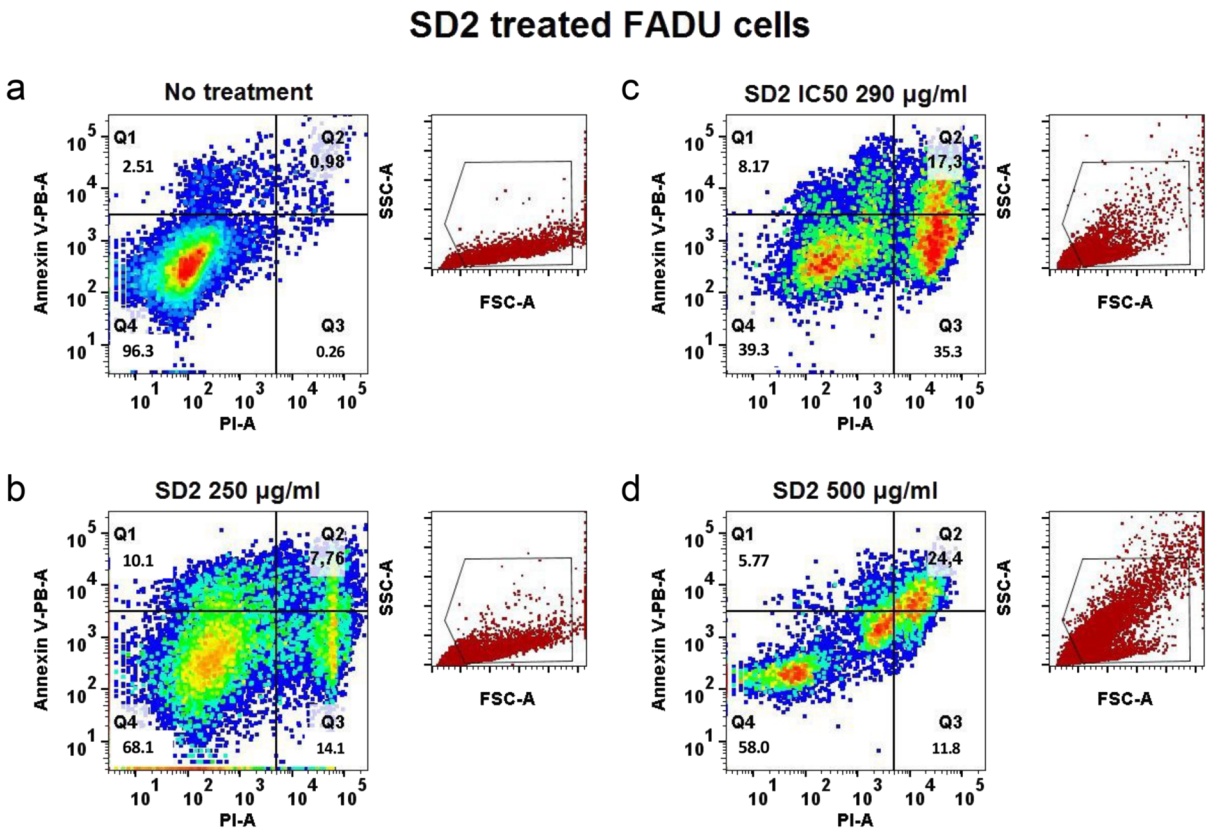

e

		Healthy	Early Apoptosis	Late Apoptosis	Necrosis
No treatment		95.3% ± 2.83%	1.75% ± 0.75%	1.83% ± 1.16%	1.12% ± 1.58%
SD2	*250 µg/ml*	**35.12% ± 24.79%** ***	13.82% ± 6.39%	**28.63% ± 18.14%** *	22.45% ± 19.23%
	290 µg/ml (IC50)	**22.34% ± 23.3%** ***	17.82% ± 8.47%	**48.18% ± 30.3%** ***	11.68% ± 14.53%
	500 µg/ml	**38.56% ± 22.84%** ***	21.91% ± 14.46%	27.84% ± 15.53%	11.66% ± 4.77%

Fig. 6. SD2 Predominantly induces late apoptosis in FaDu cells at IC_{50} concentration. FaDu cells were left (**a**) untreated (negative control) or treated for 24 h with SD2 at (**b**) 250 µg/mL, (**c**) IC_{50}-290 µg/mL, (**d**) 500 µg/mL. Results are expressed as the percentage of cells corresponding to Q1: early apoptotic cells (Annexin V^+/PI^-); Q2: late apoptotic cells (Annexin V^+/PI^+); Q3: necrotic cells (Annexin V^-/PI^+); and Q4: healthy. Cells (Annexin V^-/PI^-). Red dot blots (SSC-A/FSC-A) represent corresponding backgate. Representative example of 5 independent experiments. (**e**) The table refers to the percentage of cells corresponding to each apoptotic level (Mean ± SD). Two-way ANOVA test with Tukey correction across each row indicates statistical significance $^*p < 0.05$, $^{**}p < 0.01$, $^{***}p < 0.001$ vs. control.

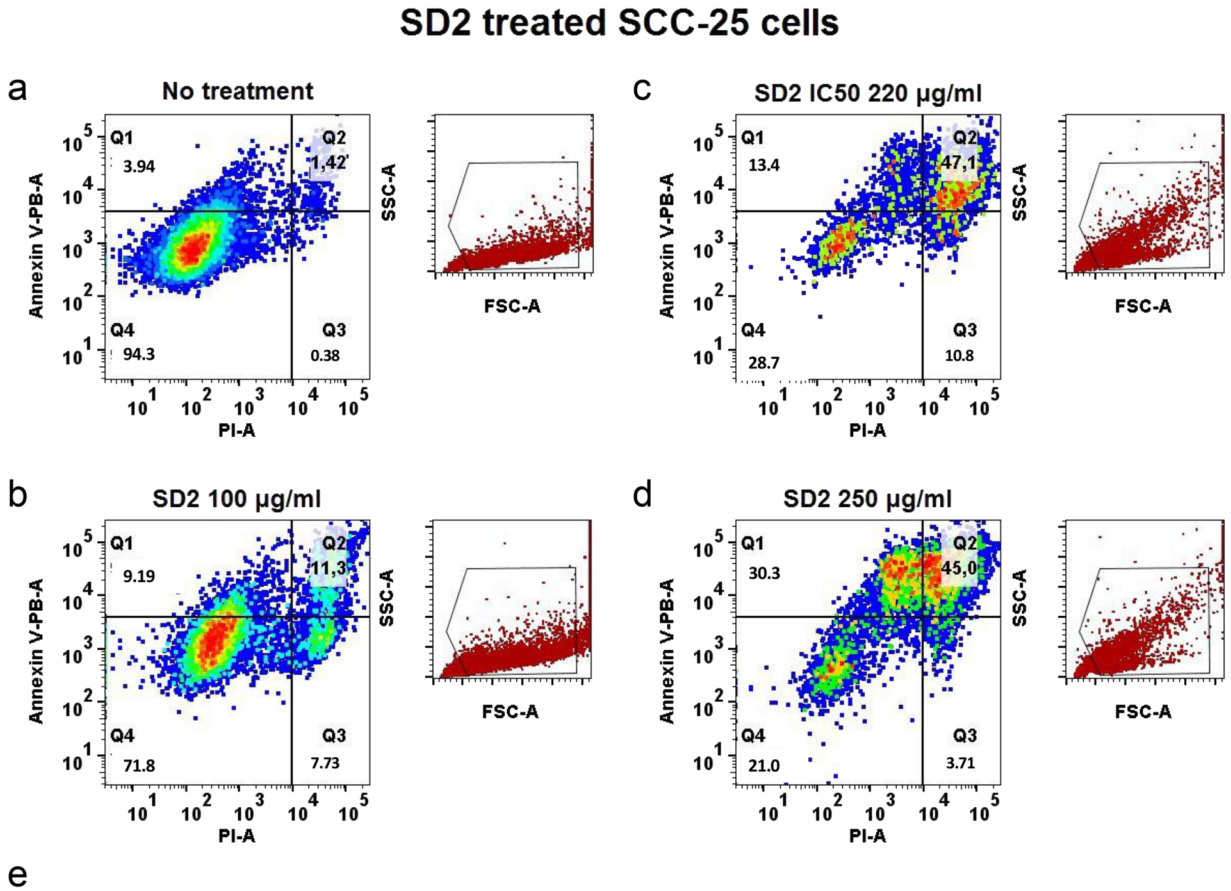

e

		Healthy	Early Apoptosis	Late Apoptosis	Necrosis
No treatment		89.28% ± 5.20%	5.36% ± 3.5%	3.84% ± 2.01%	1.63% ± 1.22%
SD2	*100 µg/ml*	**44.88% ± 35.09%** ***	9.96% ± 2.88%	**37.85% ± 31.62%** ***	6.52% ± 6.82%
	220 µg/ml (IC50)	**18.23% ± 6.99%** ***	**34.38% ± 14.32%** **	**41.53% ± 6.04%** ***	5.49% ± 4.02%
	250 µg/ml	**13.49% ± 5.45%** ***	**40.33% ± 8.03%** ***	**43.33% ± 7.14%** * **	2.29% ± 2.06%

Fig. 7. SD2 predominantly induces late apoptosis in SCC-25 cells at IC_{50} concentration. SCC-25 cells were left (**a**) untreated (negative control) or treated for 24H with SD2 at (**b**) 100 µg/mL, (**c**) IC_{50}-220 µg/mL, (**d**) 250 µg/mL. Results are expressed as the percentage of cells corresponding to Q1: early apoptotic cells (Annexin V^+/PI^-); Q2: late apoptotic cells (Annexin V^+/PI^+); Q3: necrotic cells (Annexin V^-/PI^+); and Q4: healthy. Cells (Annexin V^-/PI^-). Red dot blots (SSC-A/FSC-A) represent corresponding backgate. Representative example of 5 independent experiments. (**e**) The table refers to the percentage of cells corresponding to each apoptotic level (Mean ± SD). Two-way ANOVA test with Tukey correction across each row indicates statistical significance $^*p < 0.05$, $^{**}p < 0.01$, $^{***}p < 0.001$ vs. control.

The divergence in cellular responses observed in A253, SCC-25, and FaDu cell lines, A253 and SCC-25 displaying late apoptosis and FaDu undergoing necrosis upon interaction with IC_{50} concentration of SD2, can be attributed to a multitude of factors. This response could potentially be assign to variations in the cellular signaling pathways and inherent molecular profiles specific to each cell line. This discrepancy in the mode of cell death may arise from differences in the expression levels of key regulatory proteins involved in apoptotic and necrotic pathways, which ultimately dictate the cellular response to external stimuli such as SD2[44,45].

Flow cytometry shows the basic apoptotic profile of SD2-treated cell lines. These cell specific apoptotic profiles demonstrated in the flow cytometry analysis have led us to explore the apoptosis related gene expression profile.

Differential regulation of apoptosis-related genes by Dex-CeNPs (SD2) in HNC cell lines through RT-PCR analysis
In the present study, the expression level of pro-apoptotic (BAX, CASP3) and anti-apoptotic (Bcl-2) genes were examined in A253, FaDu and SCC25 treated with SD2 IC_{50} amount for each cell line. In addition, changes in the expression level of TP53, which is mutated in all cell lines and a key factor in the decision of DNA repair or apoptosis of the damaged cell, were also analyzed. The disparities in gene expression levels were quantified as fold changes between treated and untreated (control group) conditions, as illustrated in Fig. 8.

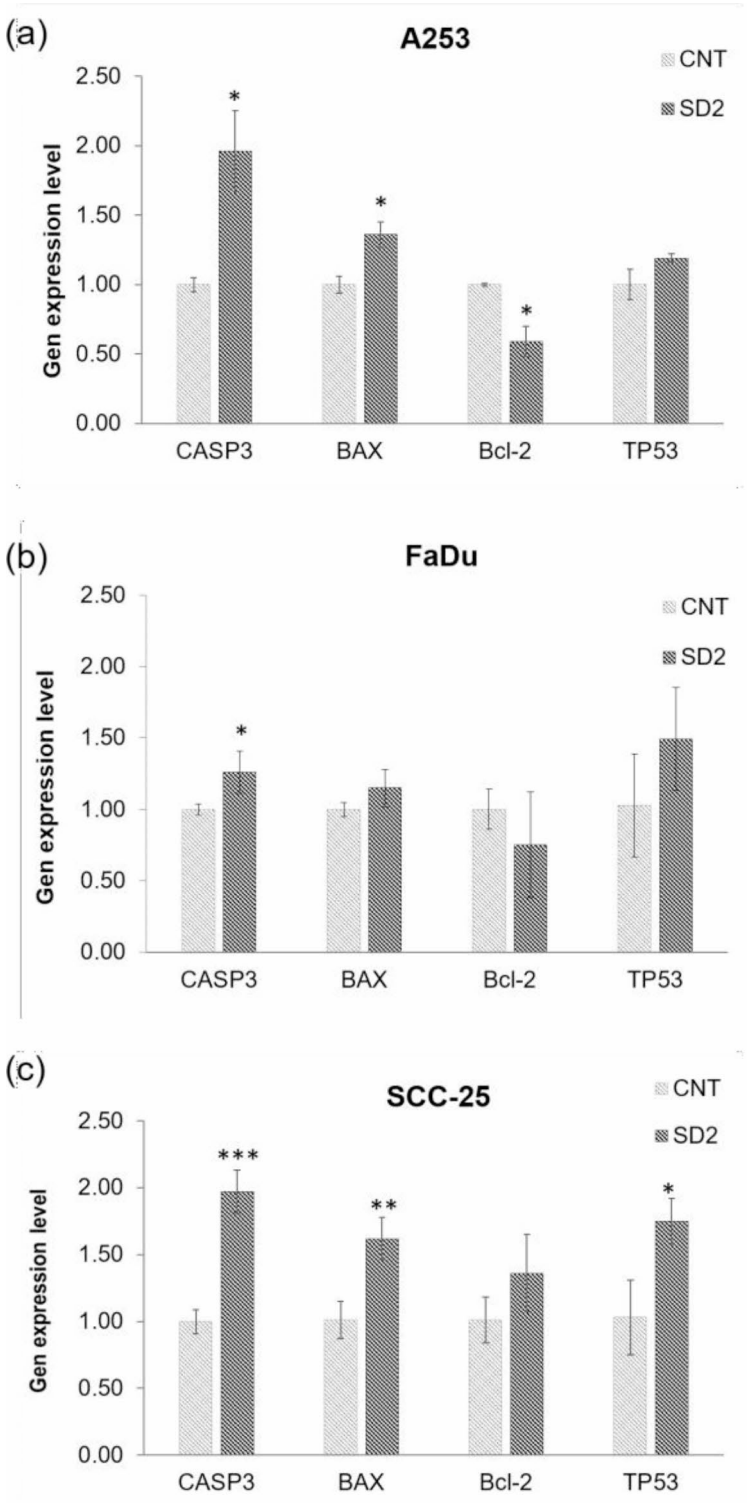

Fig. 8. (**a**,**b**) Upregulation of the pro-apoptotic genes (BAX), along with CASP3 and TP53, and downregulation of the anti-apoptotic gene (Bcl-2), demonstrating the apoptotic response induced by SD2 treatment in A253 and FaDu cells, respectively. (**c**) In the SCC-25 cell line, expression levels of all genes (BAX, CASP3, TP53, and Bcl-2) were increased following SD2 treatment at IC_{50} concentration. Signal intensities of relative genes are normalized to β-actin gene expression level. Quantitative results are presented as the mean ± SD from three independent experiments. Statistical significance was evaluated with Student t-test. $^{*}p < 0.05$, $^{**}p < 0.01$, $^{***}p < 0.001$.

In Fig. 8a, a notable upregulation in the expression of pro-apoptotic genes was observed in A253 cell line treated with SD2: CASP3 increased by approximately 2-folds, while BAX exhibited a ~ 1.4-fold increase. Conversely, the expression of the anti-apoptotic Bcl-2 gene was decreased by approximately 0.6-fold. Additionally, there was a ~ 1.2-fold increase in the expression of the TP53 gene.

As demonstrated in Fig. 8b, FaDu cell line treatment boosted pro-apoptotic CASP3, BAX and TP53 gene expression by 1.3, 1.2, and 1.5 fold, respectively, while decreasing Bcl-2 gene expression by 0.3-fold.

When the effect of SD2 synthesis was compared with the control group in the SCC-25 cell line in Fig. 8c, an increase in the expression level of all the genes was observed. The gene expression profiles of CASP3 gene (~ 2-fold), BAX gene (~ 1.6-fold) and TP53 gene (~ 1.8-fold) showed similar increasing trends consistent with other cell lines. However, the expression level of anti-apoptotic Bcl-2 gene, which has decreased gene expression level in other cell lines, increased ~ 1.8-fold in SCC-25 cell line.

As we described above, the expression levels of the TP53 and CASP3 genes considerably increased in all three cell lines after treatment of SD2. The CASP3 gene encodes a homonymous protein that acts as an effector caspase in both the extrinsic and intrinsic pathways[46]. This protein induces nucleases and proteases, causing lysis of the cell. CASP3 causes DNA damage by activating CAD-i, which causes DNA breaks in the nucleus. This effect is transmitted via the TP53 signaling pathway. The TP53 signaling pathway is known to act as an inducer in the extrinsic pathway of apoptosis. However, p53 protein, which is the product of the over-expressed TP53 gene, is localized to mitochondria and causes the initiation of apoptosis by activating BAX[47].

According to the RT-PCR results, the expression levels of the three defined pro-apoptotic genes were increased, providing further evidence for the apoptotic effect of SD2. The overexpression of pro-apoptotic genes reveal that the expression of Bcl-2 as an anti-apoptotic gene, will be reduced. Unexpectedly, in the SCC-25 cell line, Bcl-2 expression increased despite the apoptotic effect of SD2. However, BAX expression also increased in this cell line, even though Bcl-2 typically suppresses BAX. This unexpected result may explain effect of BH3 proteins on over expression of BAX[48,49].

FACS results showing that cells treated with SD2 at IC_{50} compared to the control group went to apoptosis for A253 and SCC-25. On the other hand, a high proportion of cells treated with IC_{50} of SD2 were observed in the necrosis stage for FaDu. In the case of A253, increased in expression level of pro-apoptotic genes (CASP3 and BAX) and decrease in anti-apoptotic gene (Bcl-2) was statistically significant, which is in correlation with FACS results. In the case of FaDu, we have the same expression profile with A253, but it was not that much statistically significant. Even though we have a certain amount of cells in apoptosis stage, most of the cells entered necrosis, which supports FACS data. In the subject of SCC25 cells, we have the similar FACS profile with A253 in terms of cell amounts in apoptosis stage. Moreover, statistically significant expression change in pro-apoptotic genes (CASP3 and BAX) were observed for SCC25, which supports FACS results.

Conclusion

In the current work, the application potential of cerium oxide nanoparticles coated with two distinct dextran molecules with different molecular weight and branching properties for the treatment of head and neck cancer were investigated for the first time. We successfully achieved our goals by addressing two primary objectives. Firstly, two synthesized and characterized Dex-CeNPs (SD1 and SD2) were analyzed in terms of their efficacy in HNC cytotoxicity, genotoxicity, ROS generation properties. The remarkable difference between SD1 and SD2 in terms of dextran coating was branching properties, thickness and entangled structure. The results indicate that SD2 with less branched, disentangled and thicker structure exhibits greater stability, higher Ce^{+3} ratio, lower IC_{50} values, and an increased ROS production characteristic compared to SD1. Furthermore, flow cytometry and gene expression profiles have been conducted by using SD2 due to its distinct features, which represent its applicability for future in vivo studies with clinical transition potential. Both flow cytometry and gene expression analysis show us SD2 affects head and neck cancer cells through the apoptotic pathway. Secondly, two potential nanotherapeutic candidates (SD1 and SD2) were synthesized to provide alternative candidate molecules for conjugation with various therapeutic compounds with the aim of developing molecular targeted therapy approaches in further investigations.

Materials and methods

Synthesis of dextran-coated cerium oxide nanoparticles

Two Dex-CeNPs using two different dextrans from *Leuconostoc mesenteroides* (Sigma, Cat# D9260 mol wt: 9–11 kD) (D1) and *Leuconostoc* spp. (Sigma, Cat# 31388, mol wt: ~6 kD) (D2) were synthesized through precipitation method named SD1 and SD2, respectively. The synthesis of SD1 (D1 as coating agent) and SD2 (D2 as a coating agent) was carried out according to the modified protocol published by Yazici et al.[21]. For the synthesis, 1 M cerium nitrate hexahydrate ($Ce(NO_3)_3{\cdot}6H_2O$, Sigma, Cat# 92219), 0.375 M D1 and D2 were dissolved in 2 mL dH_2O separately. 1 mL cerium nitrate hexahydrate and 2 mL dextran were mixed, and prepared solutions were added dropwise to 6 mL of a 30% ammonium hydroxide (Sigma, Cat# 221228) solution while stirring for 18 h at 25 °C. The addition of the precursor resulted in a light-yellow solution, which then turned dark brown for SD1 and dark yellow for SD2 upon the formation of stabilized Dex-CeNPs. After 18 h, particles were centrifuged at 4000 rpm for 30 min two times to eliminate the excess dextran and any large agglomerates. After centrifugation, all samples were filtered with a 0.45 µm filter before all characterization experiments. The final Dex-CeNPs solutions was stored in a refrigerator at 4 °C.

Characterization of dextran-coated cerium oxide nanoparticles

Two types of dextran-coated cerium oxide (SD1 and SD2) were characterized by using a wide range of techniques, including High Resolution Transmission Electron Microscopy (HRTEM), Fourier-transform Infrared (FTIR)

Spectroscopy, Raman spectroscopy, X-ray photoelectron spectroscopy (XPS), thermogravimetric analysis (TGA). Moreover, X-ray diffraction analysis (XRD) were performed (see Supporting Information).

UV-Vis spectroscopy
UV-Vis spectroscopy provides us quantitative information about the change in oxidation states of cerium. Before starting any measurement, a blank measurement was taken with 1 mL dH_2O (Hyclone, Cat # SH30529) in a 10 nm path-length quartz cuvette at Beckman Coulter DU800 Spectrophotometer. Later, UV-Visible spectra of all diluted samples were taken at 200–800 nm wavelength ranges.

DLS analysis
The particle size and surface charge distributions (zeta potential) of Dex-CeNPs were measuredby using DLS (Zetasizer, NanoZS, Malvern Instruments).

XPS analysis
XPS was used to determine the valence state of SD1 and SD2. XPS spectra were obtained using the PHI 5000 Versa probe (Physical Electronics, Inc., Chanhassen, MN, USA) model XPS spectrometer equipped with Al Kα X-rays (1486.6 eV) at 100 W. The data were analyzed using XPS PEAKFIT 4.1 software. Charging shifts were calibrated using C1s peak at 284.8 eV. All the peak positions matched the National Institute of Standards and Technology (NIST) XPS database. Peak fitting was performed using the standard Gaussian–Lorentzian shape function and background subtraction using the integrated Shirley method.

HRTEM analysis
High resolution transmission electron microscopy (HRTEM) analysis was used to observe particle size and morphology. It was performed with a JEOL JEM 2100 HRTEM at 200 kV. Images were taken by the Gatan Model 833 Orius SC200D CCD Camera. Carbon support film coated copper TEM grids (Electron Microscopy Sciences, CF200-Cu, 200 mesh) were used.

TGA analysis
TGA is an analytical technique to determine the thermal stability of materials by monitoring their weight change. TGA measurements of Dex-CeNPs were carried out using a TGA 6300 from SII Nano Technology, Japan, controlled by an EXSTAR 6300 controller. The sample was heated at 10 Cell/min in the temperature range of 20 °C and 825 °C in a nitrogen atmosphere.

ATR-FTIR spectroscopy
ATR-FTIR spectroscopy provides qualitative and quantitative molecular structure information, with applications ranging from monitoring processes to identifying compounds and determining components in a mixture. In this study, ATR-FTIR spectroscopy was performed to evaluate the features of Dex-CeNPs by analyzing a binding characteristic of dextran on the cerium oxide surface. For this experiment, each dextran type (D1, D2), $Ce(NO_3)_3{\cdot}6H_2O$, two synthesis types (SD1 and SD2), and each synthesis without $Ce(NO_3)_3{\cdot}6H_2O$ addition (undoped nanoparticle) were compared in liquid form throughout FTIR. All spectra were collected in Spectrum One Perkin Elmer FT-IR spectrometer, recorded at 2 cm^{-1} resolution, and averaged using 32 scans. The spectrometer operated in the spectral region between 4000 and 500 cm^{-1}.

Raman spectroscopy
Raman spectroscopy provides a structural fingerprint of Dex-CeNPs. The measurements were performed using a Renishaw in via Reflex Raman Microscopy System (Renishaw Plc., New Mills, Wotton-under-Edge Gloucestershire, U.K.). The system's wavelength was automatically calibrated against an internal silicon wafer peak at 520 cm^{-1}. The laser power was 10 mW and the exposure time was 10 s for the 532 nm diode laser. A 50× (NA:0.75) objective was used for Raman measurements.

Stability of synthesized Dex-CeNPs
The study monitored changes in absorbance, particle size, and charge characteristics of SD1 and SD2 at different time points (0, 7, 14, 21, 28, 30, 60, 120, and 180 days) to evaluate the long-term stability of the SD1 and SD2. The absorbance of both SD1 and SD2 was measured using UV-Vis spectroscopy. In contrast, DLS was used to determine changes in particle size, and zeta potential measurements were used to assess the charge characteristics of the SD1 and SD2.

Genotoxicity assay
The Ames test evaluated genotoxic properties of SD1 and SD2 according to the OECD Guideline for Testing of Chemicals: Bacterial Reverse Mutation Test (No: 471, Adopted: 21 July 1997, Corrected: 26 June 2020). For each synthesis type (SD1 and SD2), two concentrations (100 and 250 µg/mL) were used. *S. typhimurium* strains and test materials obtained from Molecular Toxicology; Inc. (Moltox) were used in this study. The information about the genotypic and phenotypic characterization of strains was given in detail in supporting information.

In vitro studies
In this study, three types of HNC cell lines, A253 (ATCC, HTB-41), FaDu (ATCC, HTB-43) and SCC-25 (ATCC, CRL-1628) were used. Their features and differences are provided in Table S1. A253 cell line was cultured in a complete medium of McCoy's 5A (Sigma-Aldrich, St. Louis, MO, USA, M930). FaDu cell line was cultured in a complete medium of EMEM (Sigma-Aldrich, St. Louis, MO, USA, M4655) SCC-25 cell line was cultured in

a complete medium of DMEM-F12 (Sigma-Aldrich, St. Louis, MO, USA, D8437). Each cell was supplemented with 10% fetal bovine serum (FBS) (HyClone, SV30160.03HI) and a 1% penicillin–streptomycin solution (1×; HyClone, SV30010). The cells were incubated at 37 °C in air supplemented with 5% CO_2 until they were 75% confluent. Following, the cells were enzymatically detached from the surface of a T-75 flask using trypsin (0.25%; HyClone) and collected by centrifugation at 1300 rpm for 5 min to proceed with all experiments.

Cytotoxicity assay

The effect of dextran-coated cerium oxide nanoparticles (Dex-CeNPs) on HNC cell viability was investigated using the Cell Proliferation Reagent WST-1 (11 644 807 001, Roche, USA). HNC cell lines (A253, SCC-25, FaDu) were seeded at 5000 cells/well in 96-well plates and allowed to adhere at 37 °C in 5% CO_2 for 24 h. The following day, cells were treated with Dex-CeNPs at 50 (not shown in figures), 100, 250, 500, and 1000 µg/mL concentrations, with media-only cells serving as controls. After a 24-h incubation with nanoparticles and discarting the old media, 100 µL of a 1:10 WST-1 reagent-cell culture media mixture was added to each well and incubated for 2 h. The absorbance of each well was measured at the 450 nm/650 nm range using Cytation 5 (BioTek, USA). WST-1 experiments were performed on both Day 1 and Day 3, and viability graphs were plotted by normalizing the data to control groups of each experiment. IC_{50} values were calculated using GraphPad. Our findings provide valuable insights into the potential therapeutic application of Dex-CeNPs for HNC treatment.

Reactive oxygen species measurement

ROS measurements were performed for one day using the 2′,7′-dichlorofluorescin diacetate (DCFDA) (Sigma Aldrich, D6883) for HNC cells. HNC cells were cultured in 96 well plates at 5000 cells/well and were allowed to adhere at 37 °C in 5% CO_2 for 24 h using respective culture media, 10% FBS, 1% penicillin/streptomycin. The following day, the cells were exposed to 100, 250, 500, and 1000 g/mL of Dex-CeNPs. As a control group, cells were cultured in media only (no Dex-CeNPs). Following 24 h of incubation with nanoparticles, ROS measurements were performed. The DCFDA dye was dissolved in 500 µL of Dimethylsulfoxide (DMSO) (Sigma, Cat#D2650) to achieve a 5 mM final concentration. The solution was vortexed until the powder was completely dissolved. 5 mM of a DCFDA solution was further diluted to 10 µM in a warm 1× Phosphate Buffer Saline (PBS) (Sigma Aldrich, 806544). After the nanoparticle treatment, cells were washed with room temperature 1× PBS two times. After washing the cells, 100 µL of 10 µM DCFDA was added to each well and incubated at 37 °C for 45 min. Fluorescence measurements were taken after 45 min using a Cytation 5 (Biotek, USA) at 485/535 nm.

Flow cytometry analysis

Annexin-V/PI immunostaining was used to analyze healthy, apoptotic, and necrotic cell ratio among Dex-CeNPs treated and untreated cells. The percentage of cells with distinct viable or dead features was measured by flow cytometry, and cells were classified as healthy (Annexin-V^-/PI^-), early apoptotic (Annexin-V^+/PI^-), late apoptotic (Annexin-V^+/PI^+), and necrotic (Annexin-V^-/PI^+). To perform cell apoptosis analysis by Flow Cytometry, A253, FaDu, and SCC-25 cell lines were treated for 24 h with SD2 particles at three different concentrations. These concentrations were selected from the five scanned concentrations and categorized as follows: the first concentration below IC_{50}, the IC_{50}, and the above IC_{50}.These concentrations were specifically determined for each cell line. Alternatively, cells were left untreated. The apoptosis rate of head and neck cell lines were visualized using Pacific BlueTM Annexin V/PI Apoptosis Detection Kit (Biolegend, Cat#640928). Following the manufacturer's instructions, cells were washed and resuspended in Annexin V Binding Buffer (1 × 106 cell/mL). Cells were stained with Pacific BlueTM Annexin V and PI respecting a ratio of Annexin V:PI 1:2. Cells were incubated for 15 min at RT in the dark and then acquired on BD FACS Canto II (BD Biosciences) instrument. All data were processed through FlowJo V10 software (BD Biosciences).

Gene expression profiling

Total RNA extraction and cDNA synthesis

Direct-zolTM RNA Miniprep Plus Kit (Cat#R2073, ZymoResearch) was used to isolate RNA. Each 6-well plate was seeded with 350,000 cells before the procedure. The seeded cells were separated into control and treatment groups. After 24 h incubation at 37 °C and 5% CO_2, the second group was treated with nanoparticles at the IC_{50} concentration specific to each cell line and then incubated again for 24 h. Subsequently, cells from the trypsinized 6-well plate were isolated. The cells were washed twice with cold PBS. Then, TRI-Reagent was added to the pellet depending on cell number and isolated using the RNA isolation technique. The 260:280 nm ratio and agarose gel electrophoresis were used to analyze the quantity, quality, and integrity of RNA samples. RNA samples were kept at − 80 °C for future studies. 1 µg of RNA was added to the procedure using the iSCript cDNA synthesis kit (BioRad Laboratories, CA, ABD, Cat# 1708891). The oligo (dT) and random primer mix reaction volume were 20 µL.

RT-qPCR analysis

SYBR Green PCR Master Mix (Bio-Rad, Cat#1725120) was used to amplify cDNA samples, which were equally diluted to 10 ng/µL. The total reaction volume of 20 µL consists of 40 ng/mL cDNA, 5mM forward and reverse primers, reaction mix and nuclease-free water. The following conditions were followed for the Real-Time PCR reaction on the AriaMx Real-Time PCR System (Agilent, USA). The DNA amplification phase, which started with the denaturation step lasting 2 min at 95 °C, was continued with 40 cycles at 95 °C for 10 s, 58 °C for 30 s, and 72 °C for 30 s. Experiments were performed with 3 biological replications for each sample. The mRNA expression levels of target genes were normalized according to the β-Actin housekeeping gene. Using the $2^{-\Delta\Delta Ct}$ technique, the relative expression of genes was determined. All designed primers were listed in supporting information.

Statistical analysis

The resulting data were statistically analyzed using the Tukey-corrected two-way ANOVA test, and the results were presented as mean values ± SD. p values < 0.05 obtained using Prism-GraphPad software, were considered significant and presented in the corresponding graph.

Data availability

The datasets generated and/or analyzed during the current study are available from the corresponding author on reasonable request.

Received: 4 September 2024; Accepted: 1 January 2025
Published online: 05 March 2025

References

1. Alsahafi, E. et al. Clinical update on head and neck cancer: Molecular biology and ongoing challenges. *Cell Death Dis.* **10**(8), 540. https://doi.org/10.1038/s41419-019-1769-9 (2019).
2. Farah, C. S. Molecular landscape of head and neck cancer and implications for therapy. *Ann. Transl. Med.* **9**(10), 915. https://doi.org/10.21037/atm-20-6264 (2021).
3. Johnson, D. E. et al. Head and neck squamous cell carcinoma. *Nat. Rev. Dis. Primers* **6**(1), 92. https://doi.org/10.1038/s41572-020-00224-3 (2020).
4. Birkeland, A. C., Swiecicki, P. L., Brenner, J. C. & Shuman, A. G. A review of drugs in development for the personalized treatment of head and neck squamous cell carcinoma. *Expert Rev. Precis. Med. Drug Dev.* **1**(4), 379–385. https://doi.org/10.1080/23808993.2016.1208050 (2016).
5. Lo, N. C., Denaro, N., Merlotti, A. & Merlano, M. Head and neck cancer: Improving outcomes with a multidisciplinary approach. *Cancer Manag. Res.* **9**, 363–371. https://doi.org/10.2147/CMAR.S115761 (2017).
6. Viegas, C., Pereira, D. S. M. & Fonte, P. Insights into nanomedicine for head and neck cancer diagnosis and treatment. *Materials (Basel)* **15**(6), 2086. https://doi.org/10.3390/ma15062086 (2022).
7. Goel, B. et al. Therapeutic approaches for the treatment of head and neck squamous cell carcinoma—An update on clinical trials. *Transl. Oncol.* **21**, 101426. https://doi.org/10.1016/j.tranon.2022.101426 (2022).
8. Chong, C. R. & Janne, P. A. The quest to overcome resistance to EGFR-targeted therapies in cancer. *Nat. Med.* **19**(11), 1389–1400. https://doi.org/10.1038/nm.3388 (2013).
9. Chai, A. W. Y., Tan, A. C. & Cheong, S. C. Uncovering drug repurposing candidates for head and neck cancers: Insights from systematic pharmacogenomics data analysis. *Sci. Rep.* **11**(1), 23933. https://doi.org/10.1038/s41598-021-03418-1 (2021).
10. Jing, Z. D., Du, Q., Zhang, X. & Zhang, Y. Nanomedicines and nanomaterials for cancer therapy: Progress, challenge and perspectives. *Chem. Eng. J.* **446**(3), 137147. https://doi.org/10.1016/j.cej.2022.137147 (2022).
11. Ruiz-Pulido, G. et al. Nanomaterials for the diagnosis and treatment of head and neck cancers: A review. *Materials (Basel)* **14**(13), 3706. https://doi.org/10.3390/ma14133706 (2021).
12. Saifi, M. A., Seal, S. & Godugu, C. Nanoceria, the versatile nanoparticles: Promising biomedical applications. *J. Control. Release* **338**, 164–189. https://doi.org/10.1016/j.jconrel.2021.08.033 (2021).
13. Barkam, S. et al. The change in antioxidant properties of dextran-coated redox active nanoparticles due to synergetic photoreduction–oxidation. *Chemistry* **21**(36), 12646–12656. https://doi.org/10.1002/chem.201500868 (2015).
14. Wang, L. et al. Shape dependence of nanoceria on complete catalytic oxidation of o-xylene. *Catal. Sci. Technol.* **6**, 4840–4848. https://doi.org/10.1039/C6CY00180G (2016).
15. Dowding, J. M. et al. Cellular interaction and toxicity depend on physicochemical properties and surface modification of redox-active nanomaterials. *ACS Nano* **7**(6), 4855–4868. https://doi.org/10.1021/nn305872d (2013).
16. Karakoti, A. S. et al. Preparation and characterization challenges to understanding environmental and biological impacts of nanoparticles. *Surf. Interface Anal.* **44**(5), 882–889. https://doi.org/10.1002/sia.5006 (2012).
17. Rajeshkumar, S. & Naik, P. Synthesis and biomedical applications of cerium oxide nanoparticles—A review. *Biotechnol. Rep. (Amst.)* **17**, 1–5. https://doi.org/10.1016/j.btre.2017.11.008 (2018).
18. Alpaslan, E., Yazici, H., Golshan, N. H., Ziemer, K. S. & Webster, T. J. pH-dependent activity of dextran-coated cerium oxide nanoparticles on prohibiting osteosarcoma cell proliferation. *ACS Biomater. Sci. Eng.* **1**(11), 1096–1103. https://doi.org/10.1021/acsbiomaterials.5b00194 (2015).
19. Naha, P. C. et al. Dextran-coated cerium oxide nanoparticles: A computed tomography contrast agent for imaging the gastrointestinal tract and inflammatory bowel disease. *ACS Nano* **14**(8), 10187–10197. https://doi.org/10.1021/acsnano.0c03457 (2020).
20. Dhall, A. & Self, W. Cerium oxide nanoparticles: A brief review of their synthesis methods and biomedical applications. *Antioxidants (Basel)* **7**(8), 97. https://doi.org/10.3390/antiox7080097 (2018).
21. Yazici, H., Alpaslan, E. & Webster, T. J. The role of dextran coatings on the cytotoxicity properties of ceria nanoparticles toward bone cancer cells. *JOM* **67**, 804–810. https://doi.org/10.1007/s11837-015-1336-5 (2015).
22. Hajareh, H. F. et al. Surface modification of TiO(2) nanoparticles with organic molecules and their biological applications. *J. Mater. Chem. B* **11**(11), 2334–2366. https://doi.org/10.1039/d2tb02576k (2023).
23. Pastuch-Gawolek, G. et al. A small sugar molecule with huge potential in targeted cancer therapy. *Pharmaceutics* **15**(3), 913. https://doi.org/10.3390/pharmaceutics15030913 (2023).
24. Perez, J. M., Asati, A., Nath, S. & Kaittanis, C. Synthesis of biocompatible dextran-coated nanoceria with pH-dependent antioxidant properties. *Small* **4**(5), 552–556. https://doi.org/10.1002/smll.200700824 (2008).
25. Li, Y. et al. Photoprotection of cerium oxide nanoparticles against UVA radiation-induced senescence of human skin fibroblasts due to their antioxidant properties. *Sci. Rep.* **9**(1), 2595. https://doi.org/10.1038/s41598-019-39486-7 (2019).
26. Costantino, F. et al. Photocatalytic activity of cellulose acetate nanoceria/Pt hybrid mats driven by visible light irradiation. *Polymers (Basel)* **13**(6), 912. https://doi.org/10.3390/polym13060912 (2021).
27. Li, C. et al. Cytotoxicity of ultrafine monodispersed nanoceria on human gastric cancer cells. *J. Biomed. Nanotechnol.* **10**(7), 1231–1241. https://doi.org/10.1166/jbn.2014.1863 (2014).
28. Hanafy, B. I., Cave, G. W. V., Barnett, Y. & Pierscionek, B. Ethylene glycol coated nanoceria protects against oxidative stress in human lens epithelium. *RSC Adv.* **9**(29), 16596–16605. https://doi.org/10.1039/c9ra01252d (2019).
29. Kaygusuz, H. & Erim, F. B. Biopolymer-assisted green synthesis of functional cerium oxide nanoparticles. *Chem. Pap.* **74**, 2357–2363. https://doi.org/10.1007/s11696-020-01084-7 (2020).
30. Mohammadi, M. R. et al. PEG/dextran double layer influences Fe ion release and colloidal stability of iron oxide nanoparticles. *Sci. Rep.* **8**(1), 4286. https://doi.org/10.1038/s41598-018-22644-8 (2018).
31. Diaconeasa, Z. et al. Cerium oxide nanoparticles and its cytotoxicity human lung cancer cells. *Rom. Biotechnol. Lett.* **20**(4), 10679–10687 (2015).

32. Farahmandjou, M., Zarinkamar, M. & Firoozabadi, T. P. Synthesis of cerium oxide (CeO_2) nanoparticles using simple CO-precipitation method. *Rev. Mex. Fís.* **62**(5), 496–499 (2016).
33. Wang, W. et al. A surfactant and template-free route for synthesizing ceria nanocrystals with tunable morphologies. *J. Mater. Chem.* **20**, 7776–7781 (2010).
34. Neal, C. J., Das, S., Saraf, S., Tetard, L. & Seal, S. Self-assembly of PEG-coated ceria nanoparticles shows dependence on PEG molecular weight and ageing. *Chempluschem* **80**(11), 1680–1690. https://doi.org/10.1002/cplu.201500237 (2015).
35. Veeragoni, D. et al. In vitro and in vivo anticancer and genotoxicity profiles of green synthesized and chemically synthesized silver nanoparticles. *ACS Appl. Bio Mater.* **5**(5), 2324–2339. https://doi.org/10.1021/acsabm.2c00149 (2022).
36. Giri, S. et al. Nanoceria: A rare-earth nanoparticle as a novel anti-angiogenic therapeutic agent in ovarian cancer. *PLoS ONE* **8**(1), e54578. https://doi.org/10.1371/journal.pone.0054578 (2013).
37. Gao, Y., Chen, K., Ma, J. L. & Gao, F. Cerium oxide nanoparticles in cancer. *Onco Targets Ther.* **7**, 835–840. https://doi.org/10.2147/OTT.S62057 (2014).
38. Nel, A. E. et al. Understanding biophysicochemical interactions at the nano-bio interface. *Nat. Mater.* **8**(7), 543–557. https://doi.org/10.1038/nmat2442 (2009).
39. Tuntland, T. et al. Implementation of pharmacokinetic and pharmacodynamic strategies in early research phases of drug discovery and development at Novartis Institute of Biomedical Research. *Front. Pharmacol.* **5**, 174. https://doi.org/10.3389/fphar.2014.00174 (2014).
40. Tang, J. L. Y., Moonshi, S. S. & Ta, H. T. Nanoceria: An innovative strategy for cancer treatment. *Cell. Mol. Life Sci.* **80**, 46. https://doi.org/10.1007/s00018-023-04694-y (2023).
41. Xu, C. & Qu, X. Cerium oxide nanoparticle: A remarkably versatile rare earth nanomaterial for biological applications. *NPG Asia Mater.* **6**, 90. https://doi.org/10.1038/am.2013.88 (2014).
42. Celardo, I., Pedersen, J. Z., Traversa, E. & Ghibelli, L. Pharmacological potential of cerium oxide nanoparticles. *Nanoscale* **3**(4), 1411–1420. https://doi.org/10.1039/c0nr00875c (2011).
43. Hanahan, D. Hallmarks of cancer: New dimensions. *Cancer Discov.* **12**(1), 31–46. https://doi.org/10.1158/2159-8290.CD-21-1059 (2022).
44. Ma, D. D. & Yang, W. X. Engineered nanoparticles induce cell apoptosis: Potential for cancer therapy. *Oncotarget* **7**(26), 40882–40903. https://doi.org/10.18632/oncotarget.8553 (2016).
45. Kumar, G., Degheidy, H., Casey, B. J. & Goering, P. L. Flow cytometry evaluation of in vitro cellular necrosis and apoptosis induced by silver nanoparticles. *Food Chem. Toxicol.* **85**, 45–51. https://doi.org/10.1016/j.fct.2015.06.012 (2015).
46. Elmore, S. Apoptosis: A review of programmed cell death. *Toxicol. Pathol.* **35**(4), 495–516. https://doi.org/10.1080/01926230701320337 (2007).
47. Taylor, R. C., Cullen, S. P. & Martin, S. J. Apoptosis: Controlled demolition at the cellular level. *Nat. Rev. Mol. Cell Biol.* **9**(3), 231–241. https://doi.org/10.1038/nrm2312 (2008).
48. Czabotar, P. E., Lessene, G., Strasser, A. & Adams, J. M. Control of apoptosis by the BCL-2 protein family: Implications for physiology and therapy. *Nat. Rev. Mol. Cell Biol.* **15**(1), 49–63. https://doi.org/10.1038/nrm3722 (2014).
49. Xu, G. & Shi, Y. Apoptosis signaling pathways and lymphocyte homeostasis. *Cell Res.* **17**(9), 759–771. https://doi.org/10.1038/cr.2007.52 (2007).

Acknowledgements

This study is supported by the International Centre for Genetic Engineering and Biotechnology (ICGEB) under CRP/TUR 18-03 project number, TUBA-GEBIP Distinguished Young Scientist Award (Hilal Yazici, 2019), Turkish Scientific and Technical Research Council (TÜBITAK) under the KAMAG-1007 Project number: 113G100.

Author contributions

E.T., S.E., J.B. and H.Y. (16. autor) wrote the main manuscript text. E.T. and F.M.B. performed nanoparticle synthesis, Stability, UV-Vis and DLS experiments, E.T. prepared Figs. 1, 2d and 3a and c, Figure S2, S.E. and K.K. performed WST1 and ROS assays, S.E. prepared Fig. 4 and Table S1, J.B. performed Gene Expression Analysis, designed primer sequences, prepared Fig. 8 and Table S2, E.T., S.E. and J.B. performed the statistical analysis. S.A. and H.Y. (9. Autor) performed Raman spectroscopy and XRD assays. They also prepared Fig. 3b and d, Figure S1., Y.T. and B.E. performed XPS assay and prepared Fig. 2a, b and S.E. and A.M.Y. performed FACS assay, A.M.Y. also prepared Figs. 5, 6 and 7 and O.D. performed HRTEM assay and prepared Fig. 2c, S.H. performed ATR-FTIR assay, F.K. and D.A.A performed Genotoxicity Assay and prepare Table S3–S10, Hu.Y. supported the preparation of the publication by obtaining and organizing the experimental results with her experience and knowledge. Hi.Y. awarded with ICGEB and TUBA funds for the project. She also carried out the scientific management of the entire process as the principal investigator.All authors reviewed the manuscript.

Declarations

Competing interests

The authors declare no competing interests.

Additional information

Supplementary Information The online version contains supplementary material available at https://doi.org/10.1038/s41598-025-85228-3.

Correspondence and requests for materials should be addressed to H.Y.

Reprints and permissions information is available at www.nature.com/reprints.

Publisher's note Springer Nature remains neutral with regard to jurisdictional claims in published maps and institutional affiliations.